2D Axisymmetric Coupled Computational Fluid Dynamics–Kinetics Modeling of a Nonthermal Arc Plasma Torch for Diesel Fuel Reforming

Alexandre Lebouvier, François Cauneau, Laurent Fulcheri

2D Axisymmetric Coupled CFD-kinetics Modeling of a Nonthermal Arc Plasma Torch for Diesel Fuel Reforming

Alexandre Lebouvier, François Cauneau and Laurent Fulcheri[*]

Center for Energy and Processes, MINES ParisTech, Rue Claude Daunesse BP 207, 06904 Sophia Antipolis Cedex, France

[*]To whom correspondence should be addressed. Phone: +33 (0)4 93 95 74 06. Fax: +33 (0)4 93 95 75 35. E-mail: laurent.fulcheri@mines-paristech.fr

Abstract

The present study is dedicated to the coupled CFD-kinetics 2D axisymmetric modeling of plasma-assisted diesel fuel reformer developed for two different applications: (i) onboard H_2 production for fuel cell feeding and (ii) NO_x trap regeneration. These cases correspond to very different reacting conditions. In the first case, diesel fuel reacts with air while in the second case it reacts with diesel engine exhaust gas. The plasma is modeled with a simple power source domain. *n*-heptane has been chosen as a surrogate molecule for diesel fuel. A reduced kinetic mechanism is used for the study. Both cases have been studied under adiabatic and nonadiabatic postreactor conditions. We can distinguish four zones in the torch: a reactant heating zone, a plasma zone, a mixing zone and a postdischarge zone. The main precursors of the reforming reactions are H, O and OH radicals. The oxygen rate is a key point of the application. The thermal losses make the reforming reaction difficult to ignite and beget a lower syngas production and a lower postdischarge temperature. For the nonadiabatic reactor, the results have been compared to experimental data. The model predicts relevant gas fractions.

Introduction

For many years, many advanced coupled CFD-kinetics models have been developed, mainly for combustion applications (O/C > 2). For instance, the development of homogeneous charge compression ignition (HCCI) engines needs a lot of knowledge on real kinetic reaction happening in the cylinder. These models are highly time-consuming and essentially depend on the size of the kinetic mechanism. For the reforming application (O/C ~ 1), recent CFD-kinetics models have been developed to study partial oxidation, steam or autothermal reforming of methane[1-4], autothermal reforming of biogas[5] or hexadecane[6] with very simple kinetic mechanism. CFD-kinetics models have been also developed for different reforming reactors: solid oxide fuel cell (SOFC)[7], membrane reformer[8], fluidized bed reactor[9] or microreactor[2,4]. Most CFD models developed for plasma torch study are non-reactive models[10,11]. A recent study by Serbin et al. has focused on a CFD-kinetics model of plasma coal gasification[12].

The literature is very poor concerning the modeling of low current – high voltage reforming plasma torches under reactive conditions[13] while experimental plasma-assisted reforming has been widely studied[14-17]. Benilov *et al.* has developed a low current plasma discharge model in atmospheric pressure to study the non-equilibrium effects[18]. Most CFD models developed for plasma-assisted reforming processes were mainly dedicated to the flow inside the torch[19,20]. Chemical reactions were not taken into account. In the first paper, the plasma is not considered and the study has been focused on the methane/air mixing at the location of the plasma. In the second one, the plasma is considered as a source term of power and the reverse vortex flow influence on the plasma is investigated. Most of the other plasma-assisted reforming numerical models are based on chemical kinetics modeling with CHEMKIN package[21], in 0D or 1D. A comprehensive review of these models is given in Ref. 13.

For several years, intensive researches have been dedicated at CEP, both experimentally and numerically, on reforming processes for two different applications (i) onboard production of hydrogen for fuel cell powering and (ii) NO_x trap regeneration, using a nonthermal arc discharge torch. Let us point out that these cases correspond to very different reacting conditions. In the first case, diesel fuel reacts with air while in the second case it reacts with diesel engine exhaust gas which is much less oxidative than air. Experimentally, we have studied the plasma-assisted reforming of gasoline[22], ethanol and E85[23] for H_2 fuel cell feeding, and the plasma-assisted exhaust gas fuel reforming of diesel fuel for a NO_x trap regeneration application[24]. Indeed, using a plasma to produce onboard reductants, such as CO and H_2, is an alternative to the classical reforming catalysts. During a regenerating period, the syngas is injected to the NO_x trap catalyst to convert the NO_x into N_2. A comprehensive description of the experimental bench and the application are given in Ref. 24.

Thermodynamics model[25], multistage kinetics model[26] and non-reactive MHD model have been devoted to plasma-assisted syngas production. These models suffer from drawbacks. The thermodynamics and multistage kinetics models consider the perfect mix of reactants and do not consider the thermal losses. The MHD model considers only air as plasma gas because, so far, it is not possible to incorporate chemical kinetic mechanism into MHD models due to the high complexity of involved mechanisms and the lack of basic kinetic data.

In order to move forward a completely integrated model, we present in this paper the simulation of a reforming plasma torch under reactive conditions. This model allows getting significant information about the mixing zone between cold and hot gas.

The plasma-assisted diesel fuel reforming model has been studied for two different applications: (i) onboard H_2 production for fuel cell feeding and (ii) NO_x trap regeneration application. Both applications have been investigated under adiabatic and nonadiabatic conditions. The results of the nonadiabatic model have been compared to the experimental

results in terms of syngas production. The experimental setup and results have been detailed in Ref. 24.

Mathematical Model

Assumptions. The two-dimensional axisymmetric model studied is based on the following main assumptions:

- The plasma is modeled as a homogeneous high-density power source under thermodynamics equilibrium and thus the non-equilibrium phenomena are not taken into account.

- The kinetic mechanism does not consider the excited or charged species.

- Gravitational effects are not taken into account.

- The gas is treated as semi-compressible. The mass density depends on temperature.

Governing Equations. The stationary conservation equations can be written in the generalized form as:

$$\vec{\nabla} \cdot (\rho \vec{v} \Phi) = \vec{\nabla} \cdot (\Gamma_\Phi \vec{\nabla} \Phi) + S_\Phi , \ (1)$$

Where ρ is the fluid mass density, v the velocity vector, Γ_Φ the diffusion coefficient, S_Φ the source term and Φ represents the scalar variable that must be solved in the various conservation equations. Φ, Γ_Φ and S_Φ are given for each conservation equation in Table 1. u, v, w, μ_l, μ_t, P are x-, y- and z-velocity, laminar viscosity, turbulent viscosity and pressure, respectively. h, λ, C_p, Pr are enthalpy, thermal conductivity, specific heat and Prandtl number, respectively. X_i is the mass fraction. k, P_k, ε, C_1 and C_2* are turbulent kinetic energy, production rate of turbulent kinetic energy, dissipation rate, 1.42 (model constant) and model non-constant coefficient, respectively. The viscosity and the specific heat depend on temperature. The thermodynamic and transport properties have been taken from the Chemkin thermodynamic[27] and transport databases[28].

The equations have been solved using the commercial CFD code Fluent v. 12.1. The SIMPLE algorithm and Pressure-based solver have been used. The ReNormalization Group (RNG) k-ε turbulence scheme has been chosen. The RNG k-ε model is a classical turbulence scheme used for swirl-dominated combustion flows. The RNG k-ε model considers several scales of turbulence, contrary to the standard the standard k-ε model which considers only one scale of turbulence. It allows guaranteeing that turbulent mixing is computed at the finest possible case regarding the mechanical conditions. As we are in the case of a rotating flow, we considered using the RNG formalism of the k-ε model as it is known to give better results in this case[29]. Both schemes are not different, as they both use a closure on the same two variables. We did not compared the quality result for the two schemes, as there is no evidence in the literature showing results should be degraded in our case.

The turbulence-chemistry interaction model is based on the Eddy Dissipation Concept (EDC). It assumes that reactions occur in the small turbulent scales, called the fine scales. We know that the EDC model may be influenced by the mixing conditions: mixing time and the fine scale fraction at the cell level. We know that specific works show the influence of this effect[30], but our goal is to evaluate, at this step, the limits and needs of classical computing schemes.

The radiations emitted by the plasma have not been taken into account because, in a developed MHD model, assuming an optically thin plasma, we have shown that the arc radiations are negligible in the energy equation compared to Joule heating and convection (about 4 orders of magnitude).

Computational grid and boundary conditions. The torch geometry is presented in Figure 1 and corresponds to a real experimental set-up, shown in Figure 2. It is composed of two separated zones: the plasma zone and the postdischarge zone with 70 mm / 4 mm and 500 mm / 11 mm length / inner radius respectively with a divergent between both zones. Let us point
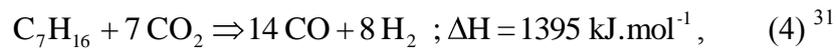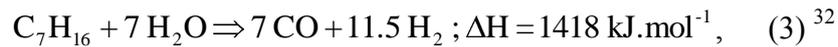
out that the plasma zone is the part where the arc plasma really takes place whereas the postdischarge zone is an active or passive zone, located downstream the plasma zone where, reactions ignited in the plasma zone continue to take place. The whole reactor domain has been meshed to obtain significant information about the entry zone, the reactive plasma zone and the mixing zone. The postdischarge has also been entirely meshed to obtain the syngas production reached at the exit in order to compare them to experiments. The grid mesh is exclusively composed of hexa-elements and contained 13 456 cells. The mesh is structured and exclusively composed of rectangles elements. In the nozzle, the mesh cells size is 0.2 mm x 0.2 mm. The number of cells is 20 in the radial direction in the whole torch. In the post-discharge zone, the mesh is released in the axial direction. The mesh is not refined at the wall. A sensibility study has been made on the mesh density and showed that our mesh was refined enough. The plasma source, modeled by a source term of power, is implemented by means of User Defined Function (UDF) in a limited zone of 1 mm / 70 mm radius / length respectively in the center of the nozzle.

The boundary conditions are detailed in Table 2. The atmospheric pressure is imposed at the outlet. Experimentally, the diesel fuel is vaporized externally by a plug flow system and then mix with the exhaust gas before entering the torch. The mix temperature measured by a thermocouple before entering the torch is about 573 K, and is used as the inlet parameter of the model. A swirl injection is applied at the inlet. The swirl allows the wall-stabilization of the plasma, the rotation of the arc root to avoid fast destruction of the electrode, and allows covering a higher reaction volume. The swirl intensity has not been evaluated. Experimentally, the flow is injected tangentially to the anode. That corresponds to an infinite swirl number. In the system, we injected a small component of the axial velocity in order to run the simulation and stay close to the experimental parameters. After the bottleneck, the swirl intensity (tangential velocity over axial velocity) varies between 1 and 2. Thus the

bottleneck leads to a strong decrease in the swirl intensity, and the boundary conditions before the bottleneck will not slightly influence the results. The injected species for both cases studied are detailed in Table 3. The first case corresponds to the partial oxidation reaction, which is highly exothermic:

$$C_7H_{16} + 7\,O_2 \Rightarrow 7\,CO + 8\,H_2\;;\Delta H = -586\;kJ.mol^{-1},\;(2)\;[31]$$
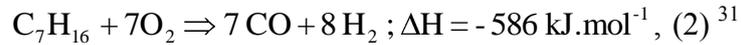
The second operating condition corresponds to a real diesel engine exhaust gas for a low engine load. The high content of H_2O and CO_2 in the plasma gas (up to 5 %) lead to energetically unfavorable conditions compared to partial oxidation commonly studied. Indeed, in addition to PO_x, the steam and dry reforming of *n*-heptane can occur and are significantly endothermic reactions. These reactions are represented by the two equations hereafter:

$$C_7H_{16} + 7\,H_2O \Rightarrow 7\,CO + 11.5\,H_2\;;\Delta H = 1418\;kJ.mol^{-1},\quad(3)\;[32]$$

$$C_7H_{16} + 7\,CO_2 \Rightarrow 14\,CO + 8\,H_2\;;\Delta H = 1395\;kJ.mol^{-1},\quad(4)\;[31]$$

Kinetic mechanism. *n*-heptane (C_7H_{16}) molecule has been chosen for calculations since it is a commonly used surrogate molecule for diesel fuel. *n*-heptane has a cetane number of approximately 54[33] which is very similar to conventional diesel fuel. This choice has been detailed in Ref. 24.

The plasma-assisted reforming process is far from combustion processes due to low amount of oxygen, O/C ~ 1 and O/C > 2 for reforming and combustion, respectively. Furthermore, due to the presence of H_2O and CO_2, the conditions of exhaust gas fuel reforming are very far from those of partial oxidation. However, the relevance of a combustion kinetic mechanism has been proven by Benilov and Naidis for low current arc discharge[34].

To avoid large computational times, a reduced mechanism of *n*-heptane, developed for combustion, has been chosen. However, reduced mechanisms are valid on a narrowest conditions range with respect with detailed mechanism. In a first step, several mechanisms[35-40] have been first tested numerically for both PO_x and exhaust gas fuel reforming conditions :

rich condition, atmospheric pressure and low temperature. The kinetic model used the Senkin module of the Chemkin II package which simulates a plug flow reactor (PFR). The model has been run for a long numerical time (~10^8 s) corresponding to the steady state. The results are checked against a thermodynamic model based T&TWinner database[41], with the same inlet molar fractions. The output data of the thermodynamic model are the species molar fractions as a function of temperature. For the outlet temperature of the Chemkin kinetic model, we compare the outlet molar fractions of the main species with the molar fractions of these species for the same temperature from the thermodynamic model.

Unfortunately, most of these mechanisms turned to be not adapted to the reforming conditions. The kinetic outlet molar fractions are very far from the thermodynamic model because of the low outlet temperature. The only kinetic mechanism, with less than 50 species and 50 reactions, which gave coherent results in terms of outlet molar fractions for exhaust gas fuel reforming conditions, is presented on Appendix A at the end of the paper. It is taken from Ref. 42 and contains 18 species and 41 reactions. No charged or excited species are considered. The kinetic mechanism does not include NO chemistry. From an energy balance point of view, nitrogen-based species will not intervene. The NOx, NH_3 and CN compound production are of course of interest regarding environmental impacts of gas emissions. Studies made with a GC-MS apparatus have shown that cyanides were in trace amounts but no ammonia was observed.

Results and discussion

First, the effect of the inlet composition has been investigated in terms of temperature, syngas production and turbulence for an adiabatic reforming torch. Then, the effects of thermal losses on kinetics evolution and temperature have been studied and compared with experimental results. N_2 is never shown for convenience reasons.

H₂ fuel cell feeding application. A first inlet composition, corresponding to the PO_x condition, has been studied in order to produce syngas which can be used in fuel cells, after a treatment unit. The input power is 1000 W. The thermal losses are not considered.

Figure 3 displays the H_2 molar fraction in the fluid domain in which we can observe a delay in H_2 production in the nozzle because of the significant temperature gradient in the radial direction. In this zone, the torch cannot be considered as a plug flow reactor. Once the flow is well mixed, this delay in conversion is not very important due to lower temperature on the axis. At the outlet, the temperature and species gradients in the radial direction are relatively low and the H_2 concentration is homogeneous in the postdischarge zone. So the results represented along the axis allow studying the phenomena occurring in the plasma zone and are representative of the postdischarge sections. Figure 4 represents the evolution of main species and temperature along the reactor axis and Figure 5 the minority species present in the first 150 mm of the torch. We can distinguish 4 distinct zones. The first zone corresponds to the heating of the reactants (C_7H_{16} and O_2). In the very beginning of the plasma zone, a strong mixing is observed due to the geometry of the plasma torch. In this heating zone, the radical densities do not vary much until an axial distance of 37 mm. Then, C_7H_{16} attains a sufficient temperature to be subjected to pyrolysis. The thermal decomposition of *n*-heptane leads to a growth of many species and radicals such as CH_3, H, OH, O which are known as playing a significant role in the reforming reactions.

The second zone begins in the middle of the plasma zone located at 44 mm from the input. Thanks to the high concentration of radicals, the reforming reactions take place in the plasma zone. In the beginning of PO_x reaction, while most of species densities decrease, we can see a bump of CH_3 and CH_3HCO which species oxidation helps the PO_x reaction to ignite by increasing quickly the temperature. The reaction 38 is ignited by the H specie produced and leads to a chain reaction dominated by reaction 1, reaction 38 and the reversed reaction 3. As

9

a consequence, we can also observe a high increase of very reactive radicals H (up to 10 %), O and OH. A sudden decrease of C_7H_{16} and O_2, and a significant increase of the temperature are observed. The significant increase of the temperature is due to the very exothermic properties of the partial oxidation reaction. The temperature in the domain is displayed in Figure 6. The decrease of C_7H_{16} and O_2 implies a sudden increase of H_2 and CO by radical recombination until the end of the plasma zone but also a small amount of H_2O. The bump of H_2O (+2.2%) is mainly due to the reactions involving OH.

The third zone, just downstream the plasma zone, is a mixing zone. In the PO_x condition, the mixing zone corresponds to the divergent zone. The hot gas coming from the plasma zone and the cold gas which pass around the plasma zone are mixed. The strong mixing downstream the plasma zone is highlighted in Figure 7 by the turbulent intensity. It leads to a significant drop of the temperature and a drop of H_2 and CO molar fractions. We can also observe a jump of H_2O production (+6.2%) and a slight increase of the CO_2 production (+1%). The steam production comes mainly from thermal decomposition of species such as CH_2O and from the reaction 40 around the arc where the temperature is around 2200 K. The radicals H, O and OH which were present only close to the axis because of high temperature needed are mixed together with other species which exist only around the plasma. As a consequence, we can observe a bump of most the minority species. As these species have a short life time, they decrease in the end of the mixing zone.

The fourth zone, downstream the mixing zone, is the postdischarge zone. The reactions ignited in the plasma zone continue to take place. Along the postdischarge zone, CO and H_2 slightly increase, H_2O and the temperature slightly decrease, and CO_2 remains constant. The reversed reaction of reaction 3 results in a slight H_2 increase and H_2O decrease. Indeed, the pre-exponential factor (A) of reaction 3 is very low and the temperature is not sufficient to increase the reaction speed. As a consequence, this endothermic reaction has a long

characteristic time which explains the observed trends. At the outlet, the H_2 and CO molar fractions reach 19% and 19.8%, respectively.

These results can be compared to the results of the 1D multistage model from Ref. 26 which use a *n*-octane detailed mechanism. The main PO_x reaction precursors are similar: H, O, OH and CH_3. The reactions follow the same scheme with a jump of these precursors just before the PO_x ignition and then a decrease of these precursors to the benefits of H_2 and CO.

The velocity profiles are shown in Figure 8. The profile near the wall has been plotted at a distance of 0.7 mm from the wall in the plasma zone (y = 3.3 mm). However, in the post-discharge zone, it corresponds to a distance of 7.7 mm from the wall. The gas is highly accelerated till 60 m/s in the injection zone because of the bottleneck. In the plasma zone, the high temperature increase leads to a very low mass density, and thus a high volumetric flow rate and velocity up to 110 m/s. Consequently, the species residence time is very low in the plasma zone. The total average residence time is comprised between 23 ms for the part of the gas going through the plasma to 30 ms for the gas passing next to the walls. In the postdischarge zone, except in the boundary layer, the velocity is homogeneous in radial direction.

NO_x trap regeneration application. Figure 9 shows the evolution of main species and temperature along the axis for the NO_x trap regeneration condition. The first zone, corresponding to the heating of the gas, is longer due to the high fractions of H_2O and CO_2 in the inflow and a higher mass flow rate. As a result, the second zone is shorter and leads to a lower temperature peak (4200 K). A part of the plasma energy is absorbed by CO_2 and H_2O, which are already oxidized species, and have a high heat capacity. As a consequence, C_7H_{16} and O_2 are not totally consumed in the second zone and a high fraction of these species appear in the mixing zone. Downstream the mixing zone, the speed of reforming reactions is lower

than in the PO_x condition. This phenomenon, already observed in Ref. 24, is due to the low concentration of oxygen in the gas leading to lower temperature.

We can distinguish two different zones in the postdischarge zone. In the first part, the PO_x reaction continues occurring, raising the temperature, and therefore accelerating the reaction. All *n*-heptane is consumed before O_2. C_7H_{16} is successively cracked into smaller hydrocarbons as C_7H_{15}, C_3H_6 and CH_3. It results in a slight increase of the temperature due to the exothermic property of oxidation. In the middle of the postdischarge zone, we get a runaway of the PO_x reaction which leads to the high increase of the temperature and syngas production. From an axial distance of 0.4 m, we can observe a slight consumption of CO_2 and H_2O and the temperature decreases. It shows that the dry and steam reforming slightly occurs in this part. A sub-mechanism of the dry reforming is modeled by the reversed reaction of reaction 15 which produces CO and OH. It is known that OH radical has a significant role in the reforming reaction ignition.

Influence of thermal losses and comparison with experimental data.

The postdischarge walls are mainly composed of ceramics mullite C530 which has a density of 2400 kg/m^3, a specific heat of 753 J.kg^{-1}.K^{-1} and a thermal conductivity of 2 W.m^{-1}.K^{-1}. The external temperature is set to 300 K. Convection is neglected. For the PO_x condition, the experimental data used for the comparison are taken from not published results. For the second case, the experimental data are taken from Ref. 24. In the latter case, the injected power has been increased to 1200 W because 1000 W are not sufficient to ignite the reforming reactions.

Figure 10 shows the evolution of main species and temperature for the PO_x condition. In order to compare both models, with and without thermal losses, this figure displays also the temperature, H_2 and H_2O fractions for the adiabatic and nonadiabatic reactor. As the thermal losses are only implemented in the postdischarge zone, we do not observe any difference in

12

the plasma zone. The temperature decreases quickly from 2200 to 1100 K downstream the mixing zone. In the end of the postdischarge zone, we observe a slight increase of H_2O molar fraction leading to a slight decrease of H_2. The thermal losses lead to a too low temperature to ignite the steam reforming reaction and lead a lower H_2 and CO production.

The results for the NO_x trap regeneration condition are shown in Figure 11. In the plasma zone, as the input power applied is higher in the nonadiabatic model, the temperature is higher and the reforming reactions occur quicker. H_2O and CO_2 reach the same values but the thermal losses lead to a decrease of syngas in the second part of the postdischarge zone. Consequently, a good insulation is needed to improve performances of the system.

The Table 4 shows the comparison of both cases with experiments. The model predicts relevant syngas fraction rates in both cases. In the PO_x condition, the difference in CO_2 production comes mainly from gas nonhomogeneity in the experimental reactor. The phenomenon is weaker in the exhaust gas reforming condition where a significant fraction of CO_2 is injected.

Even if the trends are similar for the nonadiabatic case, we observe a significant shift between the model and the experimental data for the temperature. The experimentally measured temperatures given by thermocouples are several hundreds kelvins lower than the predicted temperatures obtained by the model. One explanation is certainly linked to the fact that the thermocouples do not directly measure the gas temperature but a temperature resulting from the thermal equilibrium of the thermocouples between the convective gas temperature and the radiation exchanges between the thermocouple and the walls which are much colder than both the gas flow and the thermocouple.

Conclusions

We have successfully implemented a coupled CFD-kinetics model in order to study plasma-assisted reforming of diesel fuel in partial oxidation condition and a poor oxidative condition

13

corresponding to two different applications. The plasma torch used experimentally has been modeled. First, the study has focused on the influence of thermal losses in the reforming processes for both cases. Then, the numerical results have been compared with experimental results. Among the most important results to point out, one can quote:

- The model shows very good correlation with the experimental data in terms of H_2, CO and CO_2 outlet fractions.

- Four zones can be extracted for each case: a reactant heating zone, a plasma zone, a mixing zone and a postdischarge zone.

- The main precursors of the reforming reactions are very reactive species: atomic hydrogen (H), atomic oxygen (O) and hydroxyl radical (OH).

- O_2 and the temperature are the key points of the plasma-assisted reforming process. The higher the inlet oxygen rate, the higher the temperature, the quicker the reforming reactions, the higher the syngas production.

- The thermal losses in the postdischarge lead to a more difficult ignition of the reforming reactions and lead to the decrease of syngas production in the postdischarge zone. A good insulation of the postdischarge zone is needed to raise the performances.

The perspectives of the model are the implementation of a three-dimensional model able to better reproduce the swirl flow and the interactions with kinetics. A more detailed kinetic mechanism may be implemented depending on the growth of numerical resources.

Acknowledgments

References

(1) Amirshaghaghi, H.; Zamaniyan, A.; Ebrahimi, H.; Zarkesh, M. *Appl. Math. Mod.* **2010,** *34,* 2312-2322.

(2) Zhai, X.; Ding, S.; Cheng, Y.; Jin, Y.; Cheng, Y. *Int. J. Hydrogen Energy* **2010,** *35,* 5383-5392.

(3) Sadeghi, M. T.; Molaei, M. *Int. J. Chem. React. Eng.* **2008,** *6*.

(4) Fazeli, A.; Behnam, M. *Int. J. Chem. React. Eng.* **2007,** *5*.

(5) Xuan, J.; H., M. K.; C., D. Y.; Ni, M. *Int. J. Hydrogen Energy* **2009,** *34,* 9076-9086.

(6) Shi, L.; Bayless, D. J.; Prudich, M. E. *Int. J. Hydrogen Energy* **2009,** *34,* 7666-7675.

(7) Janardhanan, V. M.; Deutschmann, O. *Z. Phys. Chem.* **2007,** *221,* 443-478.

(8) Roses, L.; Manzolini, G.; Campanari, S. *Int. J. Hydrogen Energy* **2010,** *35,* 12668-12679.

(9) Dou, B.; Song, Y. *Int. J. Hydrogen Energy* **2010,** *35,* 10271-10284.

(10) Bauchire, J.; Gonzalez, J.; Gleizes, A. *J. Phys. III* **1997**, *7*, 829-837.

(11) Bauchire, J.; Gonzalez, J.; Gleizes, A. *Plasma Chem. Plasma Process.* **1997**, *17*, 409-432.

(12) Serbin, S. I.; Matveev, I. B. *IEEE Trans. Plasma Sci.* **2010,** *38,* 3300-3305.

(13) Petitpas, G.; Rollier, J.-D.; Darmon, A.; Gonzalez-Aguilar, J.; Metkemeijer, R.; Fulcheri, L. *Int. J. Hydrogen Energy* **2007,** *32,* 2848-2867.

(14) Ouni, F.; Khacef, A.; Cormier, J. M. *Plasma Chem. Plasma Process.* **2009**, *29*, 119-130.

(15) Bromberg, L.; Cohn, D.; Rabinovich, A.; Alexeev, N. *Int. J. Hydrogen Energy* **1999**, *24*, 1131-1137.

(16) Aubry, O.; Met, C.; Khacef, A.; Cormier, J. *Chem. Eng. J.* **2005**, *106*, 241-247.

(17) Gallagher, M. J.; Geiger, R.; Polevich, A.; Rabinovich, A.; Gutsol, A.; Fridman, A. *Fuel* **2010**, *89*, 1187-1192.

(18) Benilov, M.; Naidis, G. *J. Phys. D, Appl. Phys.* **2003**, *36*, 1834-1841.

(19) Bromberg, L., *CFD modeling of Plasmatron Methane Reformer;* Internal report, PSFC/JA-05-14, PSFC library, 2005.

(http://www.psfc.mit.edu/library1/catalog/reports/2000/05ja/05ja014/05ja014_full.pdf).

(20) Chirokov, A.; Gutsol, A.; Fridman, A.; Kennedy, L. *Proceedings of the 15th International symposium on plasma chemistry*, Orleans, 2001.

(21) Kee, R. J.; Rupley, F. M.; Miller, J. A. *Sandia National Laboratories Report*, SAND 89-8009, **1989**.

(22) Rollier, J.-D.; Gonzalez-Aguilar, J.; Petitpas, G.; Darmon, A.; Fulcheri, L.; Metkemeijer, R. *Energy Fuels* **2008,** *22,* 556.

(23) Petitpas, G.; Gonzalez-Aguilar, J.; Darmon, A.; Fulcheri, L. *Energy Fuels* **2010,** *24,* **2607**.

(24) Lebouvier, A.; Fresnet, F.; Fabry, F.; Boch, V.; Rohani, V.; Cauneau, F.; Fulcheri, L. *Energy Fuels* **2011,** *25* (3), 1034–1044.

(25) Rollier, J.-D.; Petitpas, G.; Gonzalez-Aguilar, J.; Darmon, A.; Fulcheri, L.; Metkemeijer, R. *Energy Fuels* **2008,** *22,* 1888-1893.

(26) Gonzalez-Aguilar, J.; Petitpas, G.; Lebouvier, A.; Rollier, J.-D.; Darmon, A.; Fulcheri, L. *Energy Fuels* **2009,** *23,* 4931.

(27) Kee, R. J.; Rupley, F. M.; Miller, J. A. *The Chemkin Thermodynamic Data Base,* Sandia Report #SAND87-8215B, **1987**.

(28) Kee, R. J.; Dixon-Lewis, G.; Warnatz, J.; Coltrin, M. E.; and Miller, J. A. *The Chemkin Transport Database,* Sandia Report #SAND86-8246, **1986**.

(29) Yakhot, V.; Orszag, S.A.; Thangam, S.; Gatski, T.B.; Speziale, C.G. *Phys. Fluids A* **1992**, *4* (7), 1510-1520.

(30) Rehm M.; Seifert P.; Meyer B. *Comput. Chem. Eng.*, **2009**, *33* (2), 402-407.

(31) Puolakka, K. J.; Juutilainen, S.; Krause, A. O. I. *Catal. Today* **2006,** 115, 217-221.

(32) Lutz, A. E.; Bradshaw, R. W.; Bromberg, L.; Rabinovich, A. *Int. J. Hydrogen Energy* **2004,** *29,* 809-816.

(33) Santana, R. C.; Do, P. T.; Santikunaporn, M.; Alvarez, W. E.; Taylor, J. D.; Sughrue, E. L.; Resasco, D. E. *Fuel* **2006,** *85,* 643-656.

(34) Benilov, M.; Naidis, G. *Int. J. Hydrogen Energy* **2006,** *31,* 769-774.

(35) http://www.erc.wisc.edu/modeling/modeling_index.htm

(36) F. Maroteaux ,Noel, L. *Combust. Flame* **2006,** *146*, 246–267.

(37) Peters, N.; Paczko, G., Seiser, R.; Seshadri, K. *Combust. Flame* **2002,** *128,* 38-59.

(38) Held, T. J.; Marchese, A. J.; Dryer, F. L. *Combust. Sci. Technol.* **1997** *123*,107–146.

(39) Liu, S., Hewson, J. C., Chen, J. H., Pitsch, H. *Combust. Flame* **2004,** *137,* 320-339.

(40) Tanaka, S.; Ayala, F.; Keck, J.C. *Combust. Flame* **2003**, *133*, 467–481.

(41) Pateyron, B.; Delluc, G.; Calve, N. Mec. Ind. **2005,** *6,* 651–654.

(42) Di Nardo, A.; Calchetti, G.; Giammartini, S.; Mongibello, G.; Mongiello, C. *Numerical Analysis of Liquid Fuel and Coal Water Slurry Combustion in an Innovative Reactor,* INEA Report, 2009.

(http://www.enea.it/attivita_ricerca/energia/sistema_elettrico/Centrali_carbone_rendimenti/RSE92.pdf)

Appendix A: Reduced kinetic mechanism of *n*-heptane used

```
REACTIONS CONSIDERED              A        b        E

1.  H+O2=OH+O                  2.20E+14    0.0    16800.0
2.  H2+O=OH+H                  1.80E+10    1.0     8826.0
3.  OH+H2=H2O+H                1.17E+09    1.3     3626.0
4.  OH+OH=H2O+O                6.00E+08    1.3        0.0
5.  H2+M=H+H+M                 2.23E+12    0.5    92600.0
6.  H+OH+M=H2O+M               7.50E+23   -2.6        0.0
7.  H+O2+M=HO2+M               2.10E+18   -1.0        0.0
8.  H+O2+N2=HO2+N2             6.70E+19   -1.4        0.0
9.  H+HO2=OH+OH                2.50E+14    0.0     1900.0
10. H+HO2=H2+O2                2.50E+13    0.0      700.0
11. O+HO2=OH+O2                4.80E+13    0.0     1000.0
12. OH+HO2=H2O+O2              5.00E+13    0.0     1000.0
13. H2+O2=OH+OH                1.70E+13    0.0    47780.0
14. H+O2+O2=HO2+O2             6.70E+19   -1.4        0.0
15. CO+OH=CO2+H                1.51E+07    1.3     -758.0
16. CH3+O=CH2O+H               6.80E+13    0.0        0.0
17. CH2O+H=HCO+H2              3.31E+14    0.0    10500.0
18. CH2O+M=HCO+H+M             3.31E+16    0.0    81000.0
19. CH2O+O=HCO+OH              1.81E+13    0.0     3082.0
20. OH+CH2O=HCO+H2O            7.53E+12    0.0      167.0
21. H+HCO=CO+H2                4.00E+13    0.0        0.0
22. HCO+O=CO+OH                1.00E+12    0.0        0.0
23. OH+HCO=CO+H2O              5.00E+12    0.0        0.0
24. O2+HCO=CO+HO2              3.00E+12    0.0        0.0
25. HCO+M=CO+H+M               1.60E+14    0.0    14700.0
26. CH3+O2=CH3O+O              7.00E+12    0.0    25652.0
27. CH3+OH=CH2O+H2             7.50E+12    0.0        0.0
28. CH3O+M=CH2O+H+M            2.40E+13    0.0    28812.0
29. CH3O+H=CH2O+H2             2.00E+13    0.0        0.0
30. CH3O+OH=CH2O+H2O           1.00E+13    0.0        0.0
31. CH3O+O=CH2O+OH             1.00E+13    0.0        0.0
32. CH3O+O2=CH2O+HO2           6.30E+10    0.0     2600.0
33. CH3+O2=CH2O+OH             5.20E+13    0.0    34574.0
34. CH3HCO+O=CH3+CO+OH         5.00E+12    0.0     1900.0
35. CH3HCO+OH=CH3+CO+H2O       1.00E+13    0.0        0.0
36. C3H6+O=CH3+CH3+CO          5.00E+12    0.0      454.0
37. C3H6+OH=CH3HCO+CH3         1.00E+13    0.0        0.0
38. C7H16+H=C7H15+H2           6.10E+14    0.0     8469.0
39. C7H16+O=C7H15+OH           1.60E+14    0.0     4569.0
40. C7H16+OH=C7H15+H2O         1.70E+13    0.0      957.0
41. C7H15=CH3+C3H6+C3H6        3.70E+13    0.0    28708.0
```

Table 1. Φ, Γ_Φ and S_Φ for each conservation equation.

Conservation equations	Φ	Γ_Φ	S_Φ
Mass	1	0	0
Momentum	u, v & w	$\mu_l + \mu_t$	$-\nabla P$
Energy	h	$\dfrac{\lambda}{C_p} + \dfrac{\mu_t}{Pr_{t,h}}$	0
Mass fraction	X_i	$\dfrac{\lambda}{C_p} + \dfrac{\mu_t}{Pr_t}$	0
Kinetic energy	k	$\mu_l + \dfrac{\mu_t}{Pr_{t,k}}$	$P_k - \rho\varepsilon$
Dissipation rate	ε	$\mu_l + \dfrac{\mu_t}{Pr_{t,\varepsilon}}$	$\dfrac{\varepsilon}{k}(C_1 P_k - \rho C_2 {}^* \varepsilon)$
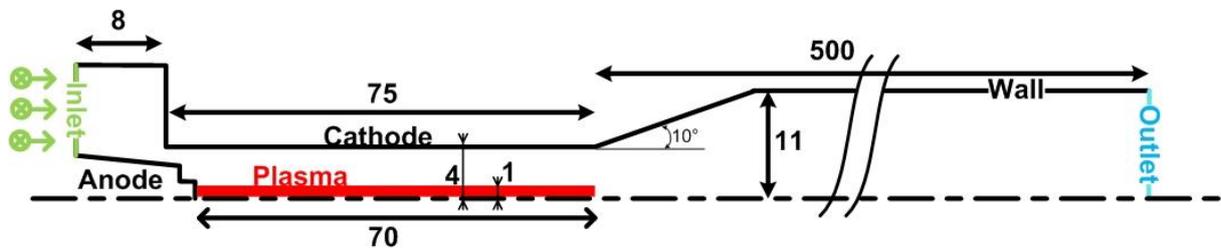
Figure 1: Scheme of the computational grid (unit: mm).
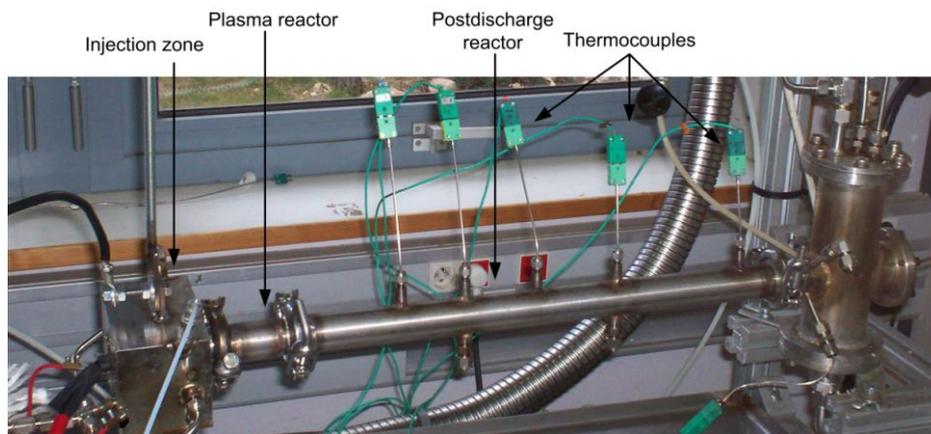
Figure 2. Photograph of the experimental set-up.

Table 2: Boundary conditions of the 2D axisymmetric model.

	Inlet	Outlet	Walls	Axis
V (m/s)	Vortex profile	$\dfrac{\partial V}{\partial n} = 0$	0	$\dfrac{\partial V}{\partial n} = 0$
T (K)	573 K	$\dfrac{\partial T}{\partial n} = 0$	$\dfrac{\partial T}{\partial n} = 0$ or $\dfrac{\partial^2 T}{\partial n^2} = 0$	$\dfrac{\partial T}{\partial n} = 0$
P (Pa)	$\dfrac{\partial P}{\partial n} = 0$	1.013×10^5	$\dfrac{\partial P}{\partial n} = 0$	$\dfrac{\partial P}{\partial n} = 0$
k (m²/s²)	k_i	$\dfrac{\partial k}{\partial n} = 0$	0	$\dfrac{\partial k}{\partial n} = 0$
E (m²/s³)	ε_i	$\dfrac{\partial \varepsilon}{\partial n} = 0$	0	$\dfrac{\partial \varepsilon}{\partial n} = 0$
Xi	Xi	$\dfrac{\partial Xi}{\partial n} = 0$	0	$\dfrac{\partial Xi}{\partial n} = 0$

Table 3: Inlet composition for the two cases studied.

Conditions	Case 1	Case 2
	PO$_x$	NO$_x$ trap regeneration
Total reactants mass flow (g/s)	0.75	1.04
C$_7$H$_{16}$ (%$_{mol}$)	5.66	3.85
O$_2$ (%$_{mol}$)	19.81	13.11
N$_2$ (%$_{mol}$)	74.53	74.12
CO$_2$ (%$_{mol}$)	0	4.16
H$_2$O (%$_{mol}$)	0	4.76
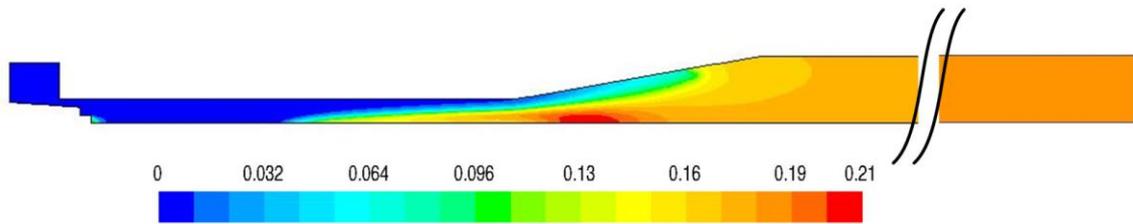
Figure 3. H_2 molar fraction in the fluid domain. PO_x condition. O/C =1. P_{plasma} = 1000 W.
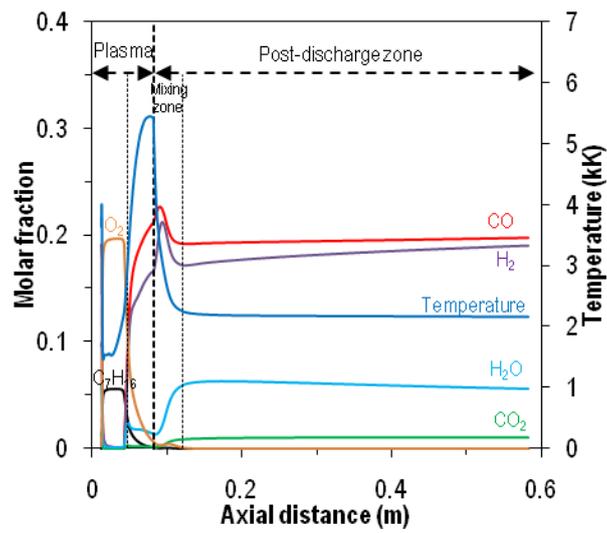
Figure 4. Evolution of the temperature and main species along the reactor axis. P_{plasma} = 1000 W.
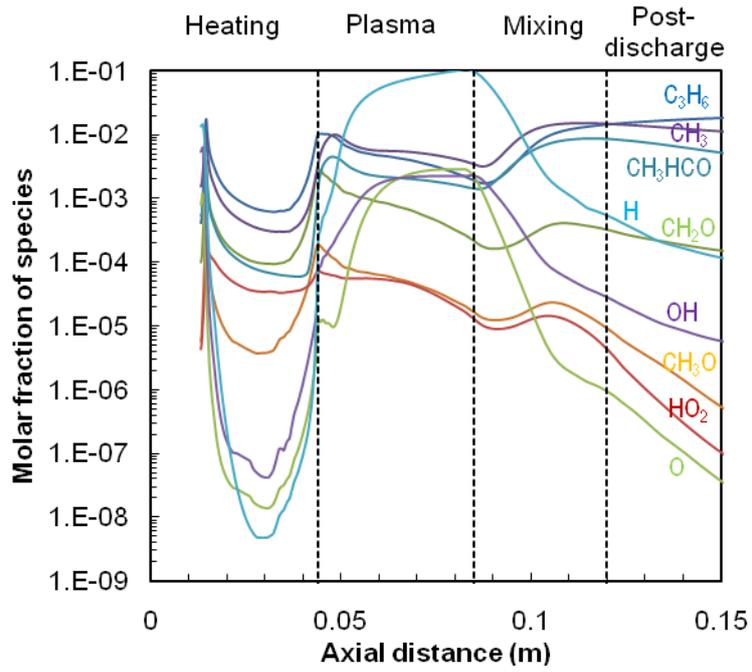
Figure 5. Evolution of the minority species in the beginning of the torch axis.
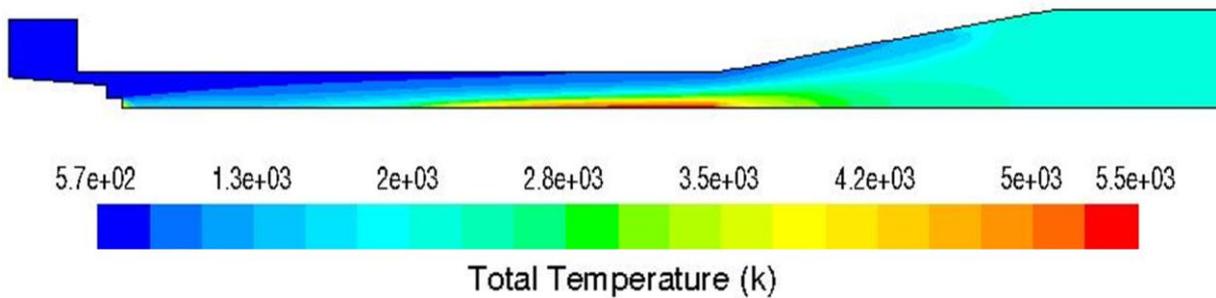
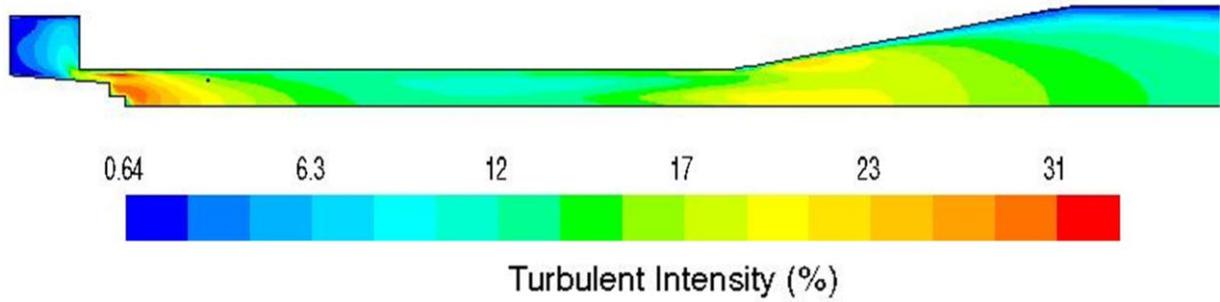Figure 6. Temperature field in the plasma zone and mixing zone. PO_x condition.

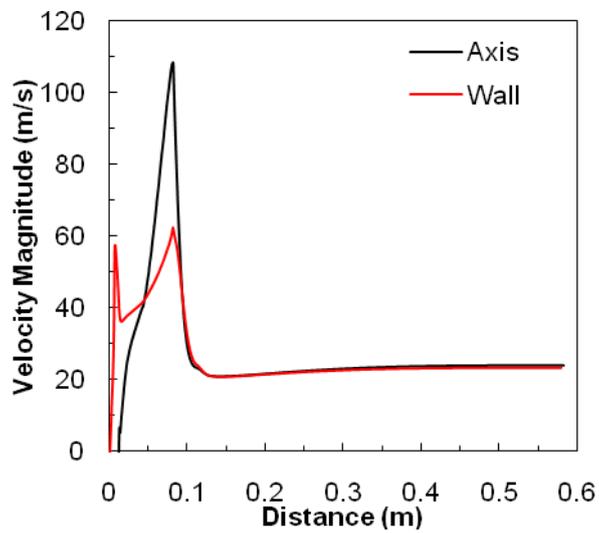Figure 7. Turbulent intensity in the plasma zone and mixing zone. PO_x condition.

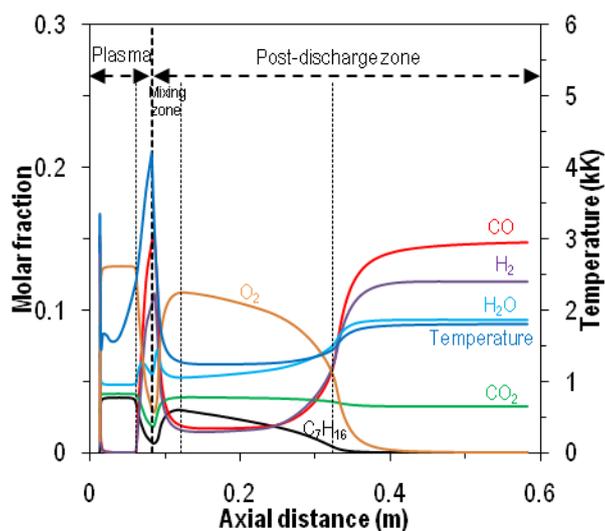Figure 8. Velocity magnitude on the axis and on a line near the cathode wall (y = 3.3 mm).

Figure 9. Evolution of the temperature and main species along the reactor axis for the NO_x trap application. $P_{plasma} = 1000$ W.
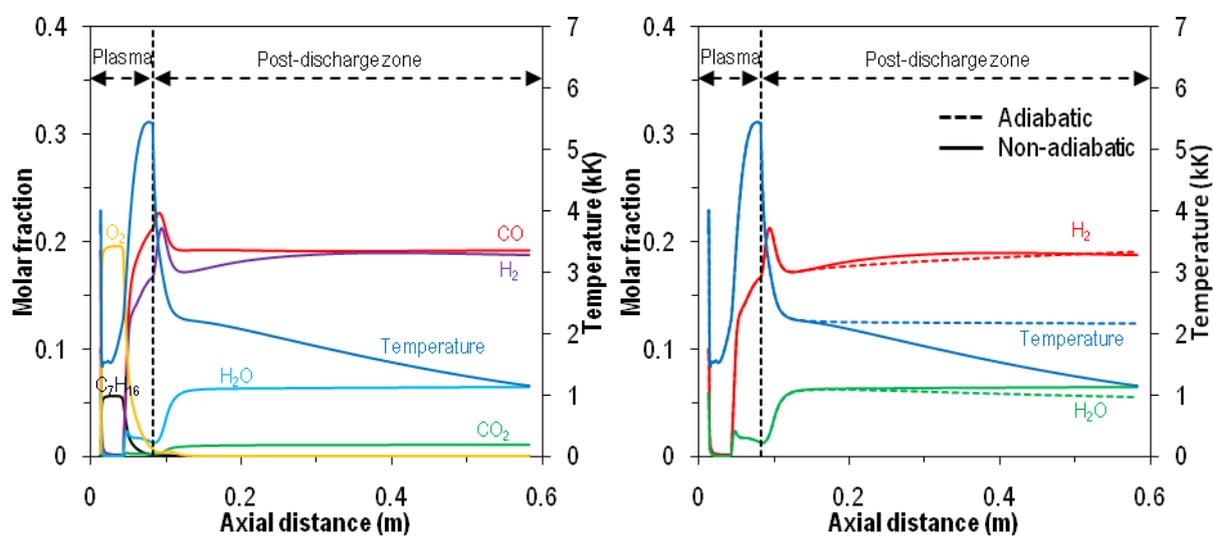

Figure 10. Evolution of the temperature and main species along the nonadiabatic reactor axis for the PO_x condition (left) and comparison with the adiabatic model (right). P = 1000 W.
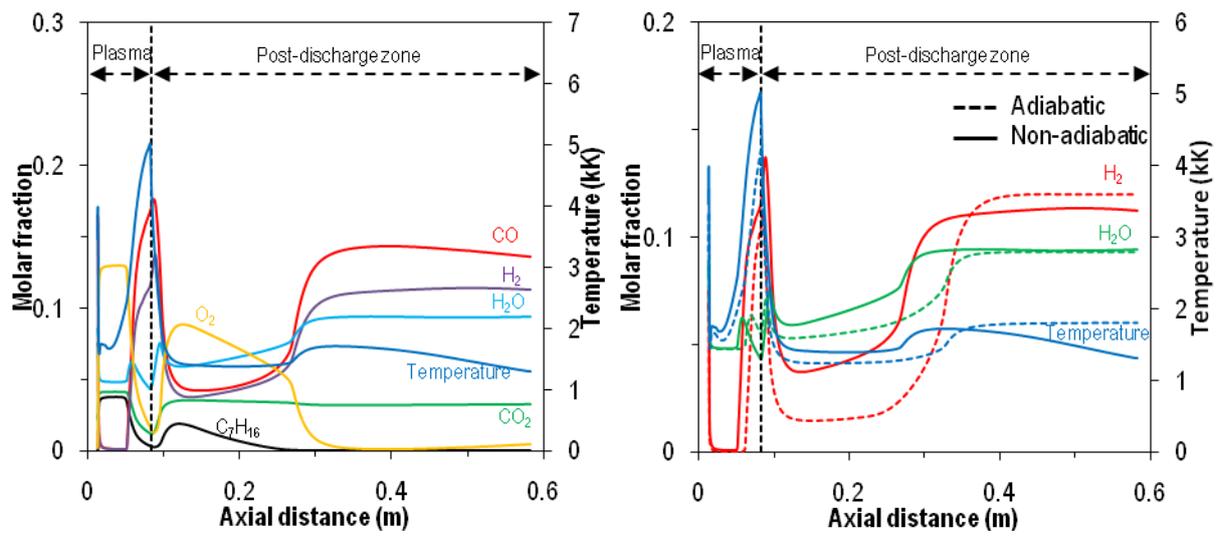
Figure 11. Evolution of the temperature and main species along the nonadiabatic reactor axis for the NO_x trap regeneration condition (left, P = 1200 W) and comparison with the adiabatic model (right).

Table 4. Comparison between 2D model and experiments. Dry molar fractions are considered.

	Case	P (W)	O/C	CO (%)	CO$_2$ (%)	H$_2$ (%)
Model	PO$_x$	800	1.2	18.7	1.42	17.3
Exp.	PO$_x$	790	1.2	18.6	2.78	14.2
Model	NO$_x$ trap	1200	1	15.7	3.8	12.9
Exp.	NO$_x$ trap	1178	1	16.0	4.1	10.8